AIAA JOURNAL
Vol. 44, No. 2, February 2006

Transverse Supersonic Controlled Swirling Jet in a Supersonic Cross Stream

S. Murugappan* and E. Gutmark†
University of Cincinnati, Cincinnati, Ohio 45221-0070
C. Carter,‡ J. Donbar,§ and M. Gruber‡
U.S. Air Force Research Laboratory, Wright–Patterson Air Force Base, Ohio 45433
and
K.-Y. Hsu¶
Innovative Scientific Solutions, Inc., Dayton, Ohio 45440

The spreading rate and mixing of a transverse jet in high-speed crossflow were modified using a swirling injector with a central control jet. The controlled supersonic swirling injector (CSSI) could be used to affect mixing both in the core and the shear layer of the jet. Rayleigh/Mie scattering from flowfield ice crystals and planar laser-induced fluorescence of the NO molecules were used to characterize penetration and mixing of the CSSI for six different cases. Instantaneous images were used to study the dynamical structures in the jet, whereas ensemble images provided information regarding the jet trajectory. Standard deviation images revealed information about the large-scale mixing/entrainment. Probability density functions were used to evaluate the probability and location of freestream, mixed, and jet fluid. They were also used to track the centerline and jet boundary on a dynamic scale. Side- (streamwise)-view images showed that the injector was capable of providing high penetration when compared to circular and swirling baseline injectors. An increase of 16% in mixing area was observed with the optimal case as compared with the other control cases. End- (spanwise)-view images show a maximum of 78% increase in total area contained within the jet boundary for the optimal case when compared to the circular injector. Higher spanwise extent of the jet boundary was also observed with controlled cases, which could provide higher interfacial area for better mixing between the jet and the cross stream when compared to their baseline counterparts.

Nomenclature

A	=	jet area
$\mathrm{CL_{TA}}$	=	centerline from the ensemble side-view images
d	=	jet diameter
J	=	momentum flux ratio, r^2
M_j	=	jet Mach number
M_∞	=	freestream Mach number
P_j	=	stagnation pressure at the upstream injection location
P_0	=	freestream static pressure
r	=	effective velocity ratio, $(\rho_j U_j^2/\rho_{\mathrm{cf}} U_{\mathrm{cf}}^2)^{1/2}$
U_{cf}	=	crossflow velocity
U_j	=	exit jet velocity
x, y, z	=	streamwise, transverse, and spanwise coordinates
Δx	=	instantaneous spanwise extent of the jet
Δx_{mean}	=	mean of Δx
Δy	=	instantaneous lateral extent of the jet
Δy_{mean}	=	mean of Δy
Δy_{std}	=	standard deviation of Δy
ρ_{cf}	=	crossflow density
ρ_j	=	jet density

Presented as Paper 2004-1204 at the AIAA 42nd Aerospace Sciences Meeting, Reno, NV, 5–8 January 2004; received 9 September 2004; revision received 16 September 2005; accepted for publication 3 October 2005. Copyright © 2005 by the American Institute of Aeronautics and Astronautics, Inc. All rights reserved. Copies of this paper may be made for personal or internal use, on condition that the copier pay the $10.00 per-copy fee to the Copyright Clearance Center, Inc., 222 Rosewood Drive, Danvers, MA 01923; include the code 0001-1452/06 $10.00 in correspondence with the CCC.

*Visiting Research Assistant Professor, Department of Aerospace Engineering. Member AIAA.
†Ohio Eminent Scholar and Chaired Professor, Department of Aerospace Engineering. Associate Fellow AIAA.
‡Senior Aerospace Engineer, Advanced Propulsion Division, 1950 Fifth Street. Associate Fellow AIAA.
§Senior Aerospace Engineer, Advanced Propulsion Division; currently Associate Professor/Coordinator, Automation and Control Technology Department, Sinclair Community College, Dayton, OH 45402-1460.
¶Research Scientist, 2766 Indian Ripple Road. Associate Fellow AIAA.

Introduction

THE scramjet propulsion concept requires rapid mixing between fuel and air due to the limited time and space available for mixing and reaction in the combustor. A major difficulty is achieving simultaneous penetration of the fuel jet into the high-speed cross-stream air and intense mixing between them, to ensure efficient combustion. Additional performance factors such as combustion efficiency, reduction of emissions, improved flammability limits, and combustion stability are all governed by the completeness of the mixing process between fuel and air.

Planar laser-induced fluorescence (PLIF) and Rayliegh/Mie scattering were employed by several investigators to visualize the turbulent nature of transverse jet injection into supersonic crossflow.[1–4] Lee et al.[1] studied reacting and nonreacting transverse jets using OH–PLIF and NO–PLIF, respectively. OH images indicated that the combustion primarily took place in the shear layer between the jet and the freestream and in the boundary layer adjacent to the wall. Hermanson and Winter[2] used Mie scattering and spark schlieren photography to visualize a nonreacting sonic jet in a Mach $M = 2$ cross stream. They observed structures that develop at the jet/freestream interface that persist far downstream in the instantaneous images. Gruber et al.[3] studied nonreacting sonic transverse injection from circular and elliptic nozzles into a supersonic flow using Rayleigh/Mie scattering. They observed axis-switching phenomena with an elliptical nozzle that enhanced the lateral spread of the jet but reduced penetration by 20% when compared to a circular injector. VanLerberghe et al.[4] reported the mixing characteristics of a nonreacting underexpanded jet in $M = 1.6$ crossflow. Counter rotating vortex pairs observed in the jet plume were identified to play an important role in enhancing mixing in the wake region downstream of the barrel shock. They also reported that time-averaged images greatly overestimated the actual level of instantaneous mixing in the flowfield. All of these studies observed large-scale structures in the

single-shot images, which were not apparent in the frame-averaged images and emphasized the need to understand the dynamic nature of the flowfield. The aim of the previous studies was primarily to understand the flow dynamics of a transverse jet (elliptical or circular jet) in a cross stream. Other investigators identified other injection schemes to enhance mixing. The following sections overview traditional fuel injection schemes and passive fuel injection strategies for scramjet applications.

There are two widely used fuel injection strategies in scramjet combustors: transverse and parallel injections. Transverse injections produce good penetration, but are inevitably accompanied by shocks that reduce the total pressure. Parallel injection, on the other hand, has lower total pressure losses and provides enhanced thrust but poor penetration and mixing into the cross stream.[5] Because of the inherent drawbacks in the two traditional injection techniques, many researchers suggested passive and active control techniques to enhance mixing at high speeds. The current work employs swirl to generate axial vorticity: hence, a brief survey of the different concepts of mixing enhancement employing vorticity generation is given. The reader is referred to Gutmark et al.,[6] Seiner et al.,[7] Bogdanoff,[8] and Bushnell[9] for more comprehensive reviews of the different experimental mixing enhancement techniques in high-speed flows.

Lobed surfaces were used to create large streamwise vortices in axisymmetric shear layers,[10,11] and ejector configurations.[12,13] This technique has been shown to improve mixing both in subsonic and supersonic flows.[12] Vorticity generated through swept and unswept ramps in supersonic flows was shown to improve mixing with higher combustion efficiency.[14,15] Dramatic differences were observed with the compression- and expansion-style ramps due to the difference is the projected stream area. For scramjet applications, the expansion-style ramps achieved higher combustion efficiency, whereas the compression-style ramps generated a stronger vorticity, which improved fuel air interface but diminished mixing.[16] Three-dimensional trailing-edge devices have also been employed to enhance shear layer three dimensionality and, consequently, enhance its mixing rate.[17,18] A 53% increase in the average mixing-layer thickness was observed with a Mach 1 helium flow and Mach 2.5 airflow by introducing a three-dimensional splitter plate with a sawtooth pattern. Most of the mixing enhancement, in this study, was also found to be on the low-speed side.[18] Tabs were also used to introduce streamwise vorticity. These devices were primarily aimed to reduce jet noise through enhanced mixing. Two distinct concepts of tabs were studied. The first introduces streamwise vorticity to enhance mixing between the two streams in the shear layer.[19–21] The second introduces large-scale shear layer instabilities through induction of additional shear layer inflection profiles.[22] Other nozzles such as tapered slot,[23] notched,[24] and splayed nozzl[25] have also been successfully employed to enhance mixing in both high- and low-speed flows.

Swirl is used in combustion systems to enhance mixing reduce emissions and provide flame stabilization in subsonic flows.[26] Swirling supersonic flows has been studied in Refs. 27 and 28. Naughton et al.[27] studied compressible jets with varying amounts of swirl. The mixing-layer growth rate obtained from the planar laser scattering technique indicated 60% increase in jet entrainment compared to the nonswirling case. They also reported high spatial extent and large-amplitude turbulent fluctuations with the addition of swirl. Kavsaoglu and Schetz[29] described the effect of swirl on mixing and penetration of a jet into crossflow from surface pressure distribution and mean velocity measurements. They observed an asymmetric pressure distribution with the effect of swirl strength being more pronounced at low velocity ratios. Swirl was also shown to reduce the penetration height and shorten the length of the potential core inducing turbulence. Niederhaus et al.[30] used PLIF to measure the planar cross sections of the swirling transverse jet in subsonic crossflow. They observed a maximum 20% decrease in penetration with addition of swirl. Swirl was also found to produce an asymmetric comma-shaped configuration as compared to the kidney-shaped behavior observed in circular jets in crossflow. Cutler and Doerner[28] studied the combined effect of swirl and injection angle of a supersonic light gas injected into a supersonic airstream. The mass fraction of the injectant obtained from a gas sampling probe in the cross stream was used to characterize mixing and penetration. A steady flow was assumed in their studies for evaluating the penetration depth and mixed mole fraction. They observed a minimal increase in mixing in the near field with a slight reduction in penetration. Both swirl and skewed injection angle had minimal effect on the mixing far downstream.

These passive control techniques could be used efficiently to improve either mixing or penetration, but their effectiveness is limited in the full operating envelope of the scramjet. Hence, there is a need for active control techniques. In the current work, an annular swirling injector with a central control jet is used to simulate a fuel nozzle. The swirling jet is injected transversely into a Mach 2 cold cross stream. It is shown that the controlled supersonic swirling ingector (CSSI) has the potential of increasing simultaneously penetration and mixing of the fuel jet with the freestream. The flowfield characteristics, penetration, spreading rate, and mixing of the CSSI in cold crossflow using Rayliegh/Mie and NO–PLIF are discussed.

Experimental Setup

The experiments were performed in the supersonic research facility at Wright–Patterson Air Force Base. The details of the wind tunnel are provided in Ref. 31. A summary of the important features is presented next.

A continuous supply of pressurized air enters the inlet section of the tunnel and flows into the settling chamber. The section houses flow conditioning and sensors to measure stagnation pressure and temperature of the freestream. The air enters into the test section (cross section 0.131×0.152 m) through a two-dimensional nozzle section at a nominal Mach number of 2. The test section has a constant-area isolator section (0.178 m long), followed by a divergent ramp (2.5 deg over 0.74 m in length).

The CSSI was used as a fuel injector in the present study. The device is compact, rugged, and simple and provides the dual benefits of high penetration and enhanced mixing. A schematic of the CSSI is given in Fig. 1a. It had two independent streams: The annular stream was used to impart swirl, whereas the central jet was used to control the penetration of the jet into the freestream and prevent early vortex breakdown. The mass flows through the annular swirl and control stream were varied in the current study. The swirl was produced through four swirl-inducing vanes. The swirl number was computed according to the following definition, taken from Ref. 32

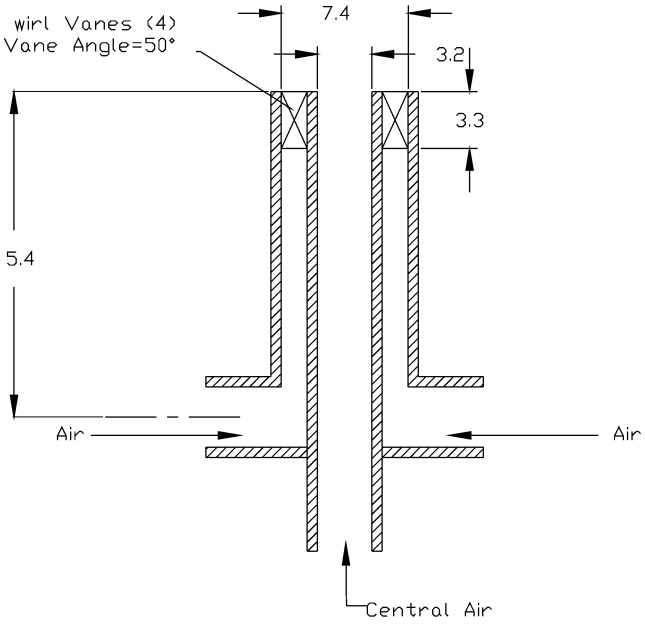

Fig. 1a Schematic of the CSSI; dimensions in millimeters.

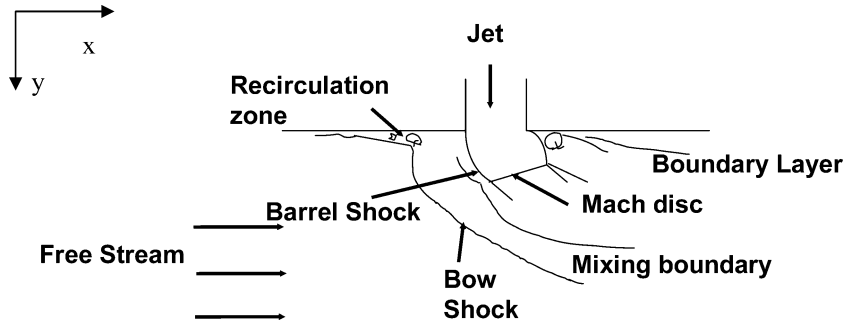

Fig. 1b Schematic of transverse supersonic jet in a supersonic crossflow.[34]

and was calculated to be 0.89:

$$\text{swirl number} = \frac{2}{3}\frac{\left[1-(D_{\text{hub}}/D_{\text{sw}})^3\right]}{\left[1-(D_{\text{hub}}/D_{\text{sw}})^2\right]}\tan\theta \qquad (1)$$

where D_{hub} and D_{sw} are the diameter of the hub and the swirler and $\theta = 50$ deg is the vanes' angle. The effective exit diameter of the CSSI was 6.1 mm. The central jet was used to energize the jet core and improve jet penetration without adversely affecting the benefits of high turbulence and mixing associated with the annular swirl stream. An earlier study by Murugappan and Gutmark[33] reported the growth rate and turbulence of the CSSI for varying levels of control at a fixed swirl number in a quiescent stream. It showed that the addition of control suppresses the turbulence in the jet core alone; also, a high-momentum flow stream was created in the jet core, which suppressed the initial jet spread, thereby providing a stable transverse jet for the CSSI as compared to a baseline swirling jet without control.

A schematic of a transverse jet injected into a cross stream is shown in Fig. 1b.[34] Figure 1b indicates the streamwise x and transverse y coordinates. The spanwise direction is perpendicular to the plane of the paper. Figure 1b also emphasizes the important flow features. The jet interacts with the crossflow producing a three-dimensional bow shock before turning downstream. A side-view shadowgraph (not shown here) show that the three-dimensional bow shock interacts with the top wall generating a reflected shock, but the jet never reached the top wall, because the top wall was approximately 25 jet diameter away from the jet exit and the maximum penetration observed was about 6 jet diameters. A separation bubble is formed upstream of the jet due to the interaction of the bow shock with the freestream boundary layer. Acceleration of the underexpanded jet into the crossflow introduces a barrel shock, which terminates at a Mach disk. A second separation region develops downstream of the jet at the boundary-layer reattachment point. The penetration of the jet has been found to be a strong function of momentum flux ratio by Papamoschou and Hubbard.[35] The transverse jet eventually spreads and mixes with the freestream fluid as it is turned by the crossflow in the streamwise direction.

Laser Diagnostics

Instantaneous measurements of the mixing regions were obtained using two methods: planar laser-induced fluorescence of NO and Mie scattering from the flowfield ice crystals. The ice crystals form naturally in the cold air from water vapor remaining in the flow stream; when performing the NO PLIF measurements, however, the air was heated enough to eliminate the formation of the ice crystals. In the Mie scattering experiments, strong scattering signals were recorded in the core flow from the small and abundant ice particles, whereas the pure injectant fluid had a low scattering signal (only background scattering) because its source was dry compressed air. In both methods, the optics/laser was tuned to the same wavelength of 226 nm. For NO–laser-induced fluorescence (LIF) detection, a single UG-5 filter was employed to block scattering at 226 nm [as well as fluorescence from the (0,0) band] and collect fluorescence from the (0,1), (0,2), (0,3), ..., bands. The blocking filter (UG-5) was removed from the charge-coupled device (CCD) camera lens to record the ice crystal scattering during the Mie scattering tests. For the NO–PLIF technique, a supply of air seeded with a stream of NO-doped N_2 (10,000 ppm NO mole fraction) was used. Uncertainty in NO concentrations was of the order of 100 ppm. The fraction of NO/N_2 in the injected airstream was relatively low, such that the net electronic quenching rate was roughly constant, regardless of the mixture fraction of the injectant.

To generate the 226-nm radiation for NO–PLIF, a Lumonics Hyperdye dye laser was pumped with the second harmonic of an injection-seeded Spectra Physics Nd: YAG laser (Model GCR-170). The dye laser output was frequency doubled using an Inrad Autotraker III. A second Autotraker III was employed in which the double-dye beam was frequency mixed with the residual Infrared beam from the Nd: YAG. The dye laser was set to a wavelength of 574 nm (to produce frequency-mixed radiation at 226 nm) to couple to the overlapped $Q_1(12)$ and $Q_2(20)$ transitions of the $A^2\Sigma^+ - X^2\Pi$ (0,0) band. The resulting pump beam linewidth was $\sim 0.1\ \text{cm}^{-1}$. To ensure good overlap of the laser and transition, a portion of the UV beam was split off and directed over a small reference flame (and then to a fast photodiode). A simple set of lenses collected and focused the resulting LIF onto the photocathode of a photomultiplier tube. This signal, along with the photodiode output, was continuously displayed on an oscilloscope, allowing minor adjustments to be made to the dye laser grating position to mitigate the effects of test cell temperature changes.

The laser sheet was formed using a pair of lenses, a plano–concave cylindrical lens (150-mm focal length) and a plano–convex spherical lens (1000-mm focal length). This arrangement resulted in a sheet height of about 50 mm. A Princeton Instruments PI-MAX CCD camera with a 512×512 pixel array was used to detect the scattering/fluorescence. The camera was fitted with a UV lens (a 45-mm/ƒ 1.8 Cerco lens) and a UG-5 Schott glass filter for NO fluorescence imaging (to block scattering at 226 nm). Note that the LIF images were not corrected for variations in collisional line broadening, electronic quenching, or ground-state population. For the end-view images, this sheet was directed across the span of the test section through fused-silica windows, and the resulting fluorescence was imaged off-normal to the sheet using a Schiempflug mount to mitigate image blur. For the side-view images, the laser sheet was directed through a fused-silica window forming the bottom floor of the wind tunnel, and the scattering/fluorescence was view in a normal-imaging configuration (Schiempflug mount not needed). The transmitting and receiving optical hardware were positioned on a traversing table allowing remote positioning of the measurement volume at any desired station in the flowfield.

Resolution of PLIF Images

The fidelity of the PLIF images depends on the image resolution and its ability to resolve the fine scalar fluctuations. The finest scalar fluctuations occur at the Batchelor scale, $\lambda_B = \beta\delta Re_\delta^{-0.75} Sc^{-0.5}$, where δ is the local jet width, β is a constant, Re_δ is the Reynolds number based on the local jet velocity, and width and Sc is the Schmidt number. Measurements in a freejet by Dowling and Dimotakis.[36] suggest β being 25. A relative resolution given as L/λ_B, where L is the largest probe dimension, was computed. It

Table 1 Operating conditions

Case	Swirl jet		Control jet		r	End-view images	Side-view images
	Flow rate, g/s	(P_j/P_0)	Flow rate, g/s	(P_j/P_0)			
A	6.1	7.11	10.2	19.11	2	Rayleigh/Mie	Rayleigh/Mie, NO–PLIF
B	9	10.45	10.2	19.11	2	Rayleigh/Mie	Rayleigh/Mie, NO–PLIF
C	6.1	7.11	5.58	10.78	1.4	Rayleigh/Mie	Rayleigh/Mie, NO–PLIF
D	6.1	7.11	0		1.1	Rayleigh/Mie	Rayleigh/Mie
E	9	10.45	0		1.4	Rayleigh/Mie	Rayleigh/Mie
F	Circular jet 10.2 19.11				2	Rayleigh/Mie	Rayleigh/Mie

was found to be 123 for $\beta = 1$ in the current study. Most of the earlier studies on compressible flow had typically a range of 100–700 (Ref. 37). Smith and Mungal[38] indicate that an $L/\lambda_B < 25$ may be considered resolved. Though the current study does not resolve the finest scales, it provides an indication of medium- and large-scale mixing.

Operating Conditions

The CSSI had two separate airstreams, one for the swirling jet and the other for penetration control. Six different operating conditions were chosen for the current study. The mass flow rates, jet pressure ratio (P_j/P_0) for the swirl and control stream, effective velocity ratio r, and laser diagnostic technique used are shown in Table 1. The error bounds in the crossflow and injection pressures were identified to be within 3% of the averaged stagnation and static pressure measurements (typically averaged over 7–8 min). This yields error bounds of 4% in blowing ratio r and less than 1% in the crossstream Mach number. Both of the injection streams were choked. Cases A–C corresponded to control cases with both swirl and control streams. The difference between cases A and C were in the amount of control stream added, whereas case A and B vary in percentage of swirl mass flow rate. Cases D and E correspond to different swirling stream flow rates without control. Case D corresponds to the baseline swirl case for cases A and C. Case E was used as a baseline swirl case for case B. Case F represents a regular circular jet. At least 150 images were acquired for each case. Each of these raw images was corrected for background and flat field variations (laser sheet variations). Analysis was performed on instantaneous and time-averaged end- (spanwise-) and side- (streamwise)-view images. The images are presented in gray scale with white representing the highest signal intensity corresponding to pure jet fluid and lowest signal intensity and black pure freestream fluid. The images were not temporally correlated. In each of the images x, y, and z corresponded to the streamwise, transverse, and spanwise directions, respectively, and the origin is at the center of the jet exit .

Results and Discussion

Side-View Images

Figure 2 shows an instantaneous side-view image of the CSSI in a $M = 2$ crossflow for case A. The shape and outline of the barrel shock and Mach disk are indicated. It was observed from the instantaneous images that the barrel shock was unsteady in nature. Similar unsteadiness in the barrel shock was also noted in Ref. 4. Small eddies that were found on either side of the barrel shock grew in size in the downstream direction along the jet's edges. The flow accelerated as it exited out of the nozzle through an expansion wave and was then compressed through a barrel shock and a Mach disk. Immediately downstream of the Mach disk, the flow decelerated and high signal intensity was observed due to the increased jet fluid density. The trajectory of the jet was highly turbulent with jet shear layer vortices visible on both the windward and leeward sides of the jet. Downstream of the Mach disk, streaks of high and low signal intensity, which occurred randomly, were visible in all instantaneous images. Figure 3a shows the time-averaged contours for case A. Similar features to those of the instantaneous images, such as size and shape of the barrel shock and Mach disk, are visible in the average contours.

Figure 4 shows the trajectory of the windward boundary of the jet for all cases from Rayleigh/Mie scattering measurements. This

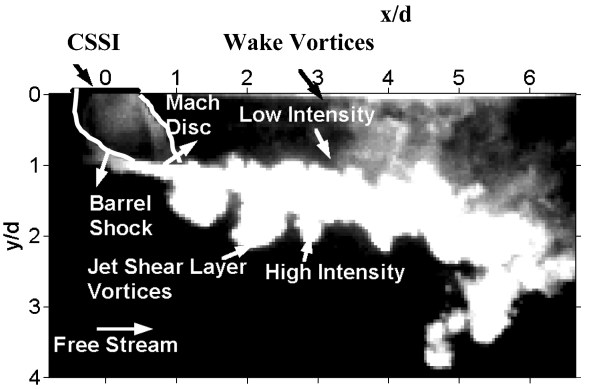

Fig. 2 Instantaneous NO–PLIF side-view image for case A.

boundary of the jet was identified from the time-averaged images as the location that corresponds to 10% of the freestream intensity. An error of ±5 pixels is associated with the detection of the jet boundary, and this translates into a maximum of 6% error in the rd scale. The plot was scaled by the product r and d. Cases A–C used the d and r of the control jet, whereas cases D and E used d and r of the swirl jet for normalization.

The $r \cdot d$ length scale was used in Ref. 39 to collapse the centerline jet trajectories at different r using the correlation

$$x/(r \cdot d) = A \cdot (y/r \cdot d)^m \tag{2}$$

The constant A and the coefficient of the exponent m were used by several other researchers to scale their data.[1–3,35,38,39] Though the data showed a power-law trend, both A and m were found to vary between experiments. The $r \cdot d$-scaled trajectories did not collapse the data for the different cases. Smith and Mungal[38] also observed that their data did not collapse for $r = 5$–25 in incompressible-flow test cases. Figure 4 also shows the data points of the upper boundary trajectory identified in compressible flow studies by Gruber et al.[3] at $r = 1.7$, $M_j = 1$, and $M_\infty = 1.98$; Wang et al.[40] at $r = 0.823$, $M_j = 1.0$, and $M_\infty = 1.21$; and Papamoschou and Hubbard[35] at $r = 2.8$, $M_j = 2.1$, 2.8, and 3.5, and $M_\infty = 2.0$. The present circular jet data (case F) agrees well with Ref. 3. Both the baseline cases D and E, which corresponded to swirling flow without control, exhibited the least penetration, indicating that swirl reduces penetration. Cutler and Doerner[28] also observed a drop in penetration with the addition of swirl. Control cases *A–C* show higher penetration when compared to the swirling baseline cases. Case A had a steady increase in penetration depth until $5.8\ r \cdot d$. The jet trajectory for case A was lower than the circular injector case F until $3.8\ r \cdot d$ but the growth rate steadily increased for control case A, whereas case F stabilized. There was a 58% improvement in slope $(\Delta y/\Delta x)$ with case A over the circular case F. The difference between cases A and C was in the amount of control stream. Case A, which possessed higher control authority, showed stronger penetration, whereas case C, which had lower mass flow on the control stream, had a lower penetration. The impact of adding more swirl had an adverse effect on penetration. Cases A and B had the same amount of control flow, but case B was turned more quickly by the crossflow in the streamwise direction as compared to A. The windward jet boundary for case B did not grow past $3.25\ r \cdot d$.

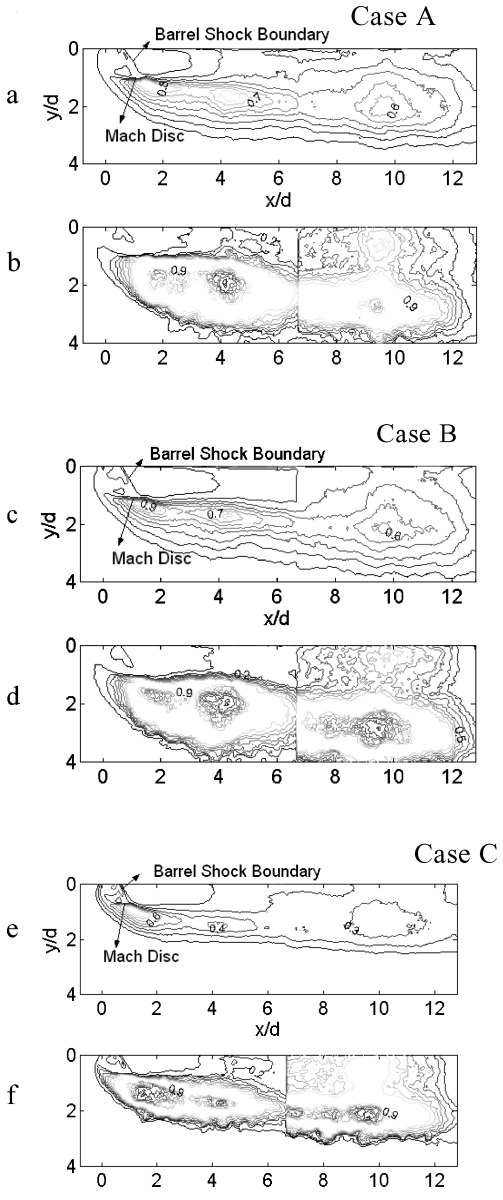

Fig. 3 Time-averaged NO–PLIF contours: a), c), and e) side views for cases A, B, and C, respectively; standard deviation NO–PLIF images: b), d), and f) side views for cases A, B, and C, respectively.

Figure 5 shows the intensity values normalized by the maximum intensity for the control cases A–C along the jet centerline. The jet centerline was identified from the location of the maximum intensity value. For each of the cases, three distinct local maxima were identified. An underexpanded jet exiting into a quiescent flow would have alternating regions of maxima and minima density, indicating the compression–expansion regions; the jet exiting into cross flow showed an alternating rise and decay of signal intensity along the jet centerline. When no pressure effect on the NO fluorescence quantum efficiency is assumed, the intensity values would be directly proportional to the number density of NO molecules along the centerline. A high signal value would then correspond to presence of high-density jet fluid that occurs through compression of jet fluid. The second intensity maxima for case C dropped to 50%, whereas it remains above 75% for cases A and B. This indicates that jet fluid was compressed more in cases A and B as compared to case C; hence, the former two cases would have stronger shock strength when compared to case C. The signal levels dropped to less than 10% of the maximum intensity for all of the cases in the third local intensity maxima region, signifying that shock exhibited much weaker compression strength.

Figures 3a–3f show the time-averaged contours and the standard deviation images (side view) for the control cases A–C using NO–PLIF. The standard deviation images for all cases show a low intensity in the barrel shock region, indicating a low degree of fluctuation compared to the jet downstream. Three distinct low-intensity regions are observed in the standard deviation images for all of the control cases. These regions correspond to the high signal levels in the time-averaged images, which represent high-density jet fluid. Narrower jet width and smaller penetration depth for case C

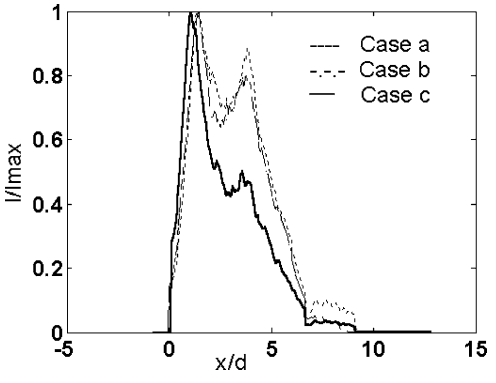

Fig. 5 NO–PLIF normalized intensity along jet centerline.

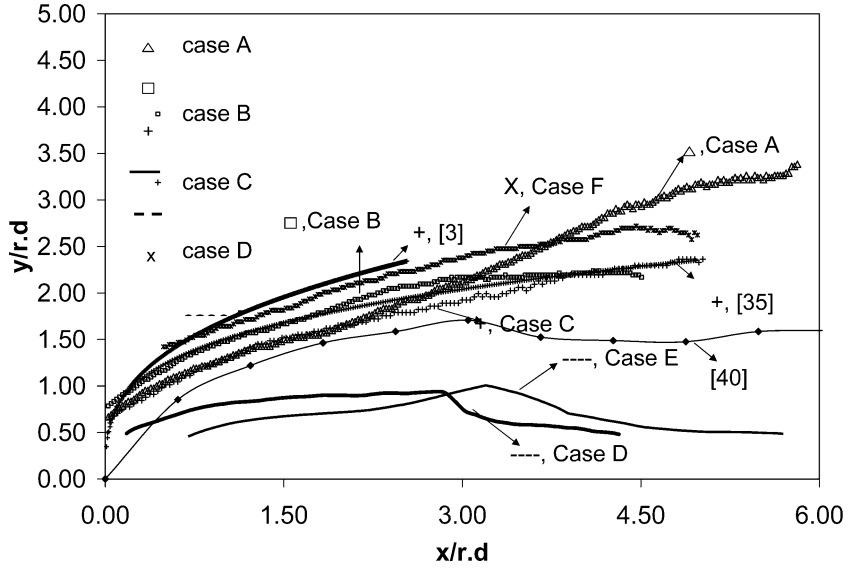

Fig. 4 Mie scatter windward jet boundary normalized by $r \cdot d$.

was observed when compared to cases A and B. Standard deviation images show higher fluctuations near the wall beginning at 8 jet diameters for case C, whereas cases A and B show similar fluctuation levels past 10 jet diameters. To quantify the large-scale mixing of the three cases, an area was computed from the standard deviation images that represent a standard deviation value of 30% or greater ($A_{\sigma,30}$). The area that contains this region is involved in either large- or small-scale mixing. Because the small-scale mixing occurs at length scales below the pixel dimension ($\delta x = \delta y = 0.27$ mm), it is difficult to distinguish between the two processes. However, it at least shows a potential of becoming molecularly mixed. Figure 6 shows the mixing area enclosed by 30% standard deviation or greater, normalized by the control jet exit area, for the three control cases at the two regions. The first region covers up to 7.4 swirling jet diameters, and the second extends from 7.4 to 13.6 swirling jet diameters. Cases A and B show higher mixing potential than case C for both regions. Cases A and B have comparable area for the region that covers 7.5 jet diameters. Case B shows 16% increase in normalized area as compared to case A, signifying higher potential to get enhanced molecular mixing farther downstream.

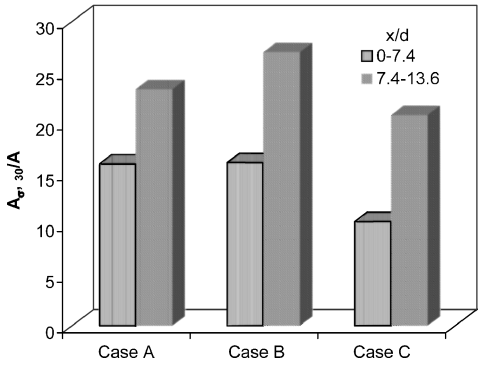

Fig. 6 NO-PLIF, mixing region area ratio.

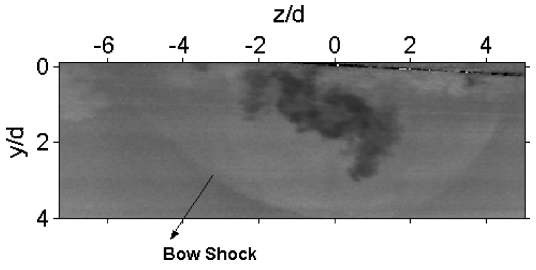

Fig. 7 Instantaneous Mie scatter end-view image at $x/d = 10.3$ for case B.

End-View Images

Figure 7 shows an instantaneous end-view image for case A at $x/d = 10.3$. Figure 7 shows the turbulent nature of the jet with large-scale structures present around its periphery. The three-dimensional bow shock visible in the time-averaged and standard deviation frames (Figs. 8) could also be identified in the instantaneous image. Figures 8a–8l show the time-averaged and standard deviation end-view images (ice crystal scattering) for the three control cases at $x/d = 4.1$ and 10.3. The apex of the bow shock at $x = 4.1d$ is higher than at $x = 10.3d$ for all control cases. The radius of the bow shock was larger as the jet exited into the crossflow due to the high momentum of the transverse jet, but the crossflow turned the jet in the streamwise direction downstream, as the jet mixed with the crossflow, losing its momentum; hence, the radius of the bow shock decreased. Both the standard deviation and time-averaged images indicate a skewed and elliptical structure for case B. A skewed boundary could also provide higher contact area between the jet fluid and freestream for enhanced mixing. The boundary enclosed by the jet in cases A and C was less skewed in the transverse direction than case B. Studies by Cutler and Doerner[28] showed a similar asymmetry for a swirling jet in supersonic crossflow.

Three different parameters were used to quantify the mixing characteristics at different streamwise locations. The mean spanwise extent Δz_{mean} of the jet boundary, mean area contained within the boundary, A_{mean}, and standard deviation of the spanwise extent of the transverse boundary, Δz_{std}. These were obtained from 200 instantaneous images at three streamwise locations for every case. Figure 9 shows the jet boundary for a typical end-view instantaneous image defining the different parameters. As with the earlier discussed side-view penetration profiles, these contours correspond to intensity values equal to 10% of the averaged freesteam intensity downstream of the bow shock. An error of ± 5 pixels (± 0.79 mm) is associated with the uncertainty in the determination of the jet edge. Figures 10a–10c shows the bar plots of the different parameters for

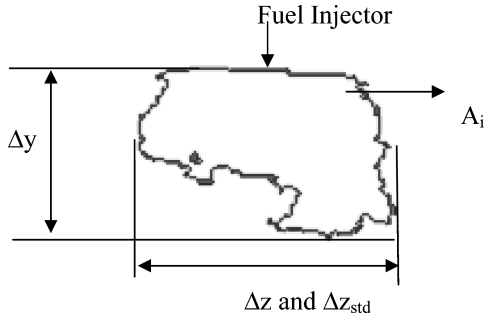

Fig. 9 Typical jet boundary from instantaneous end-view image from Mie scatter; A_{mean} = mean of A_i where i is instantaneous end-view image.

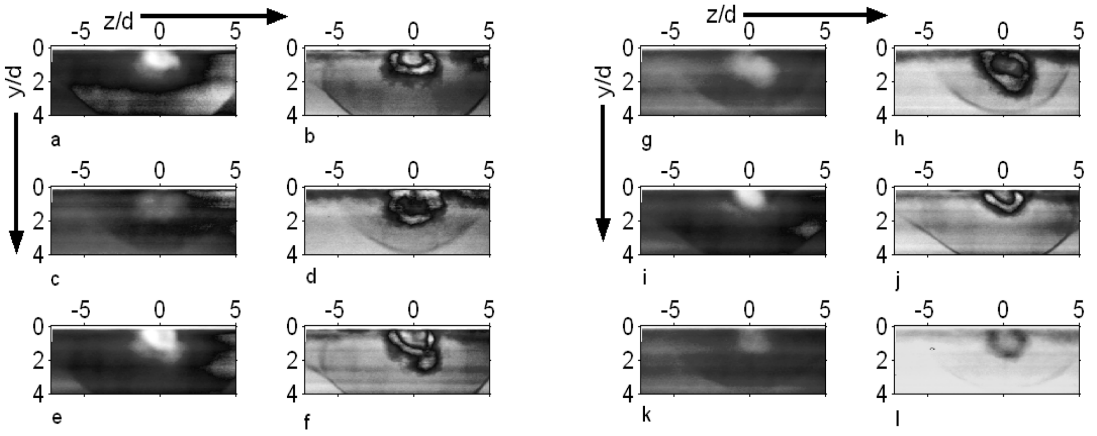

Fig. 8 Mie scatter end view: a), e), i) and c), g), k) time-averaged for cases A, B, C, at $x = 4.1d$ and $10.3d$, respectively; b), f), g) and d), h), l) standard deviation for cases A, B, C, at $x = 4.1d$ and $10.3d$, respectively.

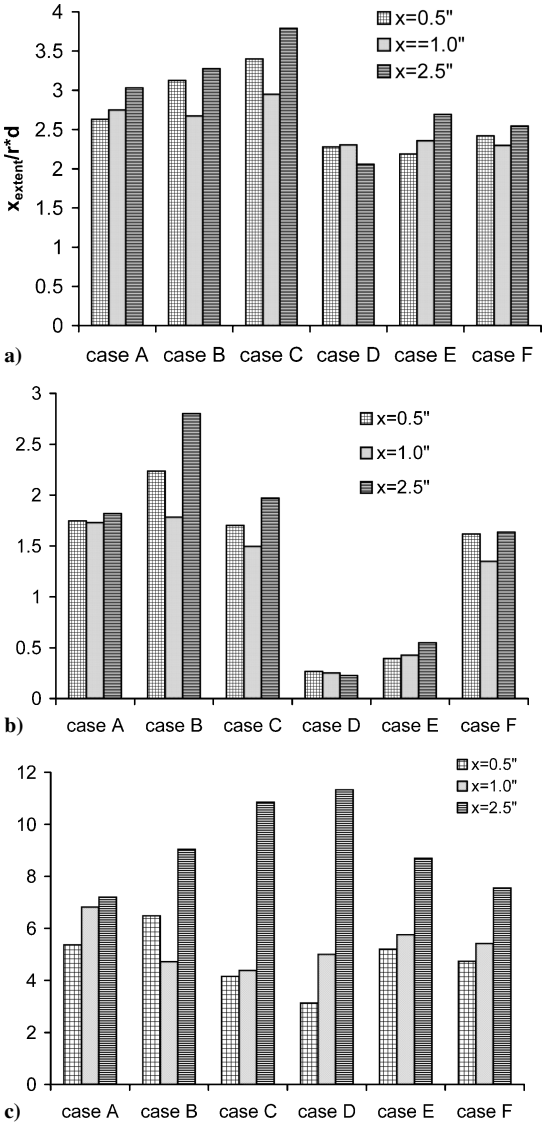

Fig. 10 Bar graphs of different mixing parameters for all cases from Mie scatter: a) $\Delta z/r \cdot d$, b) normalized mean area within jet boundary, $A_{mean}/r \cdot A$, and c) Δz_{std}.

all six cases. Figure 10a shows the bar graphs of the lateral extent of the jet boundary normalized by the product of r and d. All of the control cases show an increase in jet width when compared to the baseline swirling cases and circular jet. This indicates that the controlled case has higher potential of entraining/mixing with the freestream due to the stretching of the jet boundary. Figure 10b shows the mean area A_{mean} contained within the jet boundary. The area was normalized by the product of r and A to include the effect of blowing ratio r. A was the control jet exit area, except for the swirl cases D and E, where A corresponded to the annular swirling jet area. Note that the normalized area was also found to be higher at all of the x locations corresponding to the control cases as compared to other baseline cases. A maximum of 72% increase in area was obtained with case B as compared to circular jet, case F. This represents the potential of finding jet/mixed fluid over a larger spatial extent. This would provide higher interfacial contact between the jet and the freestream, and, hence, enhance mixing between the two streams. Figure 10c shows a bar plot of the standard deviation of the spanwise extent, Δz_{std}. This denotes the variation of the spanwise extent of the jet from the instantaneous frames. Cases A and B showed higher unsteadiness on the boundaries when compared to the other cases in the near field ($X = 0$ and 25.4 mm). Except for the circular case F, all of the others showed a larger standard deviation in the spanwise extent in the far field. This could be due to the enhanced mixing associated with swirl, which was present in varying amounts in cases A–E.

Probability Density Function Analysis

The instantaneous flowfield shows the dynamic nature of the flowfield, which is crucial in understanding the mixing processes for different cases.[1–4] The presence of large- and small-scale structures, which play an active role in flow interaction, development, and growth of the jet in cross stream cannot be observed in the time-averaged field. Probability density functions (PDFs) have been used as a tool to identify the transport characteristics of compressible mixing layers.[41–44] A passive scalar PDF measures the probability of occurrence of all mixture fractions at various locations within the mixing layer. One key concern in measuring the PDF of a mixing flow is the probe resolution. The resolution of the probe should be finer than the diffusion scales to prevent ambiguity in measuring the correct mixture fraction because any signal indicative of a well-mixed fluid could result from an average of unmixed fluid when the resolution is coarse. Such disparities between probe resolution and the flow scales are beyond the capabilities of the many optical diagnostic techniques at high Reynolds numbers (see Ref. 41).

The PDFs of signal intensities were calculated at various locations in the flowfield for the side-view images from NO–PLIF. These PDFs show the probability of occurrence of specific signal intensity at a flowfield location. Because the signal intensity is directly proportional to the number density of NO molecules in the jet fluid, the PDFs provide an indication of the mixture fraction at various locations on a pixel-sized basis. Though this cannot be used to quantify mixing at a molecular scale, it could be used to characterize the probability of large-scale mixing on a pixel basis.

The individual PDFs were constructed from the discrete intensity histograms at each location. At each location in the flowfield, 200 samples from the 200 instantaneous images were used to construct the PDFs. The intensity values were normalized by the maximum intensity on the centerline from 200 instantaneous images at every axial location. Probabilities of 1 and 0 would correspond to complete jet fluid and freestream fluid, respectively. The integration of the area under the PDF at every location equals unity, by definition.

PDF Results and Discussion

Side-View PDFs

Figures 11–13 are contour plots of the PDF for the three control cases A, B, and C at three axial locations, $x/d = 2.2$, 4.6, and 10.5, in the flowfield. The x and y axes represent the normalized intensity (ranging from 0 to 1) and transverse location, respectively. The value of each contour represents the probability of finding a certain level of (I/I_{max}). Black and white color contours correspond to low and high probability density values, respectively. The centerline location (CL_{TA}) obtained from the time-averaged side-view images is indicated as a horizontal line. There is a high probability of finding high-density jet fluid near the centerline. This probability is reduced on either side of the jet away from the centerline. Visual observations indicate that the centerline identified from time-averaged images does not coincide with the transverse location that has a probability corresponding to 1(only high-density jet fluid) for several PDFs contours, for example, cases B and C at $x/d = 2.2$. PDFs give a measure of centerline on a dynamic scale. It takes into account the variation of the intensity values from different instantaneous frames, whereas the time-averaged images indicate the centerline trajectory based on mean intensity values. An average intensity could smear the centerline due to outliers (values that correspond to high or low intensity that occur occasionally) hence; the PDF could provide a more appropriate estimate of the centerline location. Figure 14 shows the centerline location obtained from the PDFs and time-averaged side-view images. Note that the trajectory identified by the PDF is higher than that from the time-averaged images. Kamotani and Greber[45] and Hainu and Ramaprian[46] show that the trajectory obtained from maximum local velocity penetrates 5–10% deeper into the flow than the corresponding scalar concentration trajectory obtained from time-averaged images. Hence, a trajectory obtained from a dynamic analysis might closely follow that of the velocity trajectory. The jet's windward and leeward boundaries could also

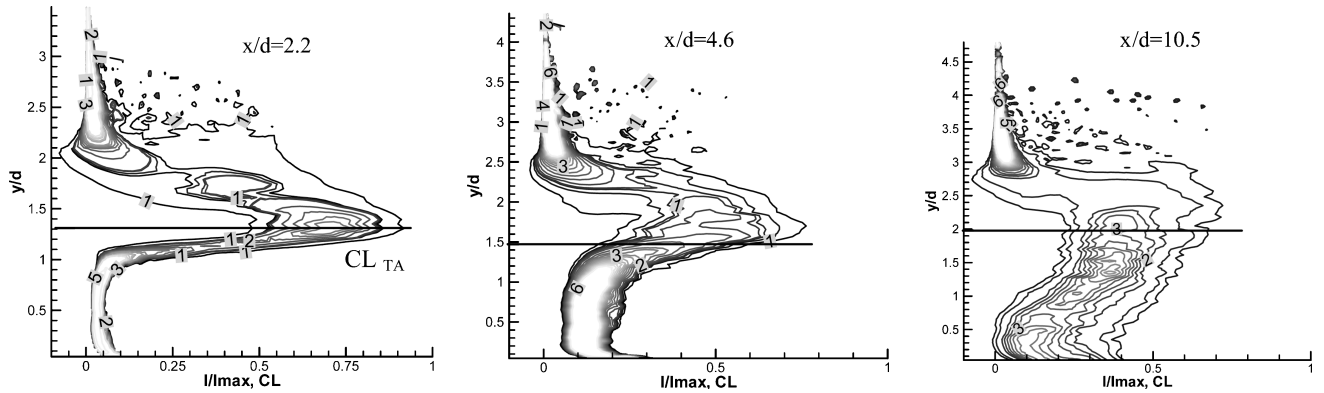

Fig. 11 PDF contour of mixture fraction for case A at three streamwise locations.

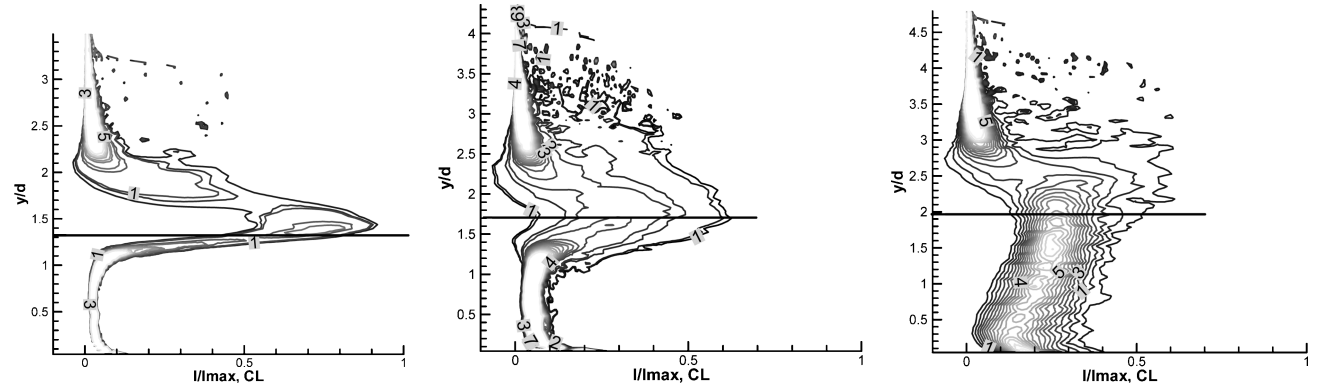

Fig. 12 PDF contour of mixture fraction for case B at three streamwise locations.

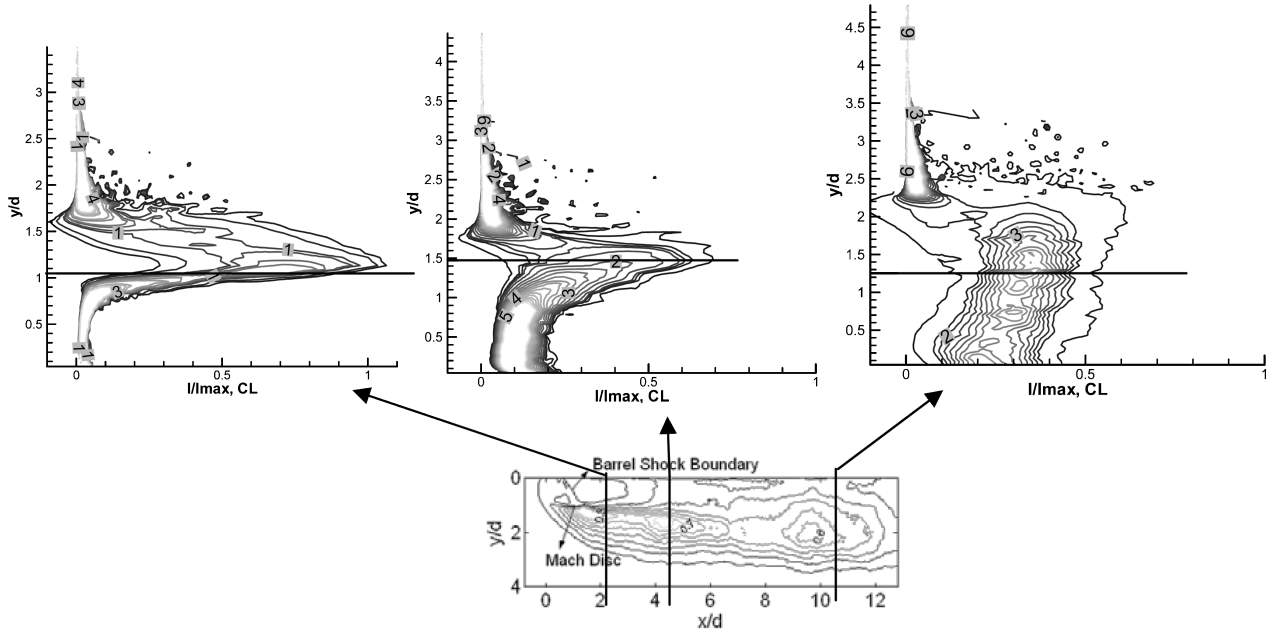

Fig. 13 PDF contour of mixture fraction for case C at three streamwise locations from NO–PLIF.

be identified from PDF contours because these would correspond to finding high probability of freestream intensity (zero for pure freestream fluid) away from the jet. The probability contours tapered more sharply immediately downstream of the bow shock, $x/d = 2.2$ toward the leeward side, indicating a well-defined jet boundary. As the jet developed, it mixed and entrained cross-stream fluid, giving a higher probability of finding mixed fluid at the downstream locations on the leeward side of the barrel shock. For all control cases, the jet had high probability of finding mixed fluid just above and below the centerline at $x/d = 2.2$. The probability contours were more sparsely placed from the centerline to the windward jet boundary for all control cases with intensities varying from 0 to 1 at $x/d = 2.2$. This indicates occasional presence of freestream, mixed, and jet fluids. At $x = 4.6d$, case B shows almost an equal probability of finding mixed fluid above and below the centerline, whereas cases A and C shows probability of identifying all values between 0 and 1.

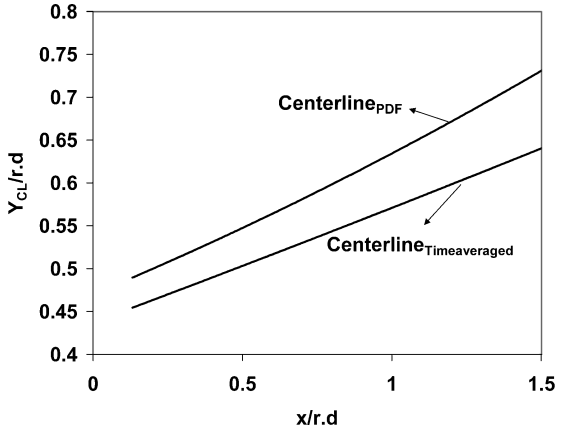

Fig. 14 Comparison of centerline trajectory from PDF contours and time-averaged images for case A from NO–PLIF.

This indicates a well-mixed region for case B, whereas cases A and C show an intermittent nature with the presence of jet, mixed, and freestream fluids. The signal intensity at $x/d = 10.5$ is below 60% maximum intensity, indicating the jet fluid is fairly mixed with the freestream for all of the cases. Also note that most of the mixed fluid with high probability is below the jet centerline. The core in case C at $x/d = 2.2$ shows a mixture of probabilities varying from 0 to 1 near the core of the jet, whereas cases A and B, shows a condensed and narrow core. This feature indicates a high probability of jet fluid near the centerline in cases A and B, whereas case C shows an intermittent nature with the freestream penetrating the jet core. At $x/d = 10.5$, all cases show occasional tongues of high-probability jet fluid above the jet centerline.

End-View PDFs

Figures 15a–15d show the end-view PDF contours at four different transverse locations, $y/d = 0.31$, 0.94, 1.2, and 1.6, for case B. There is an unequal probability of mixture fraction on the two

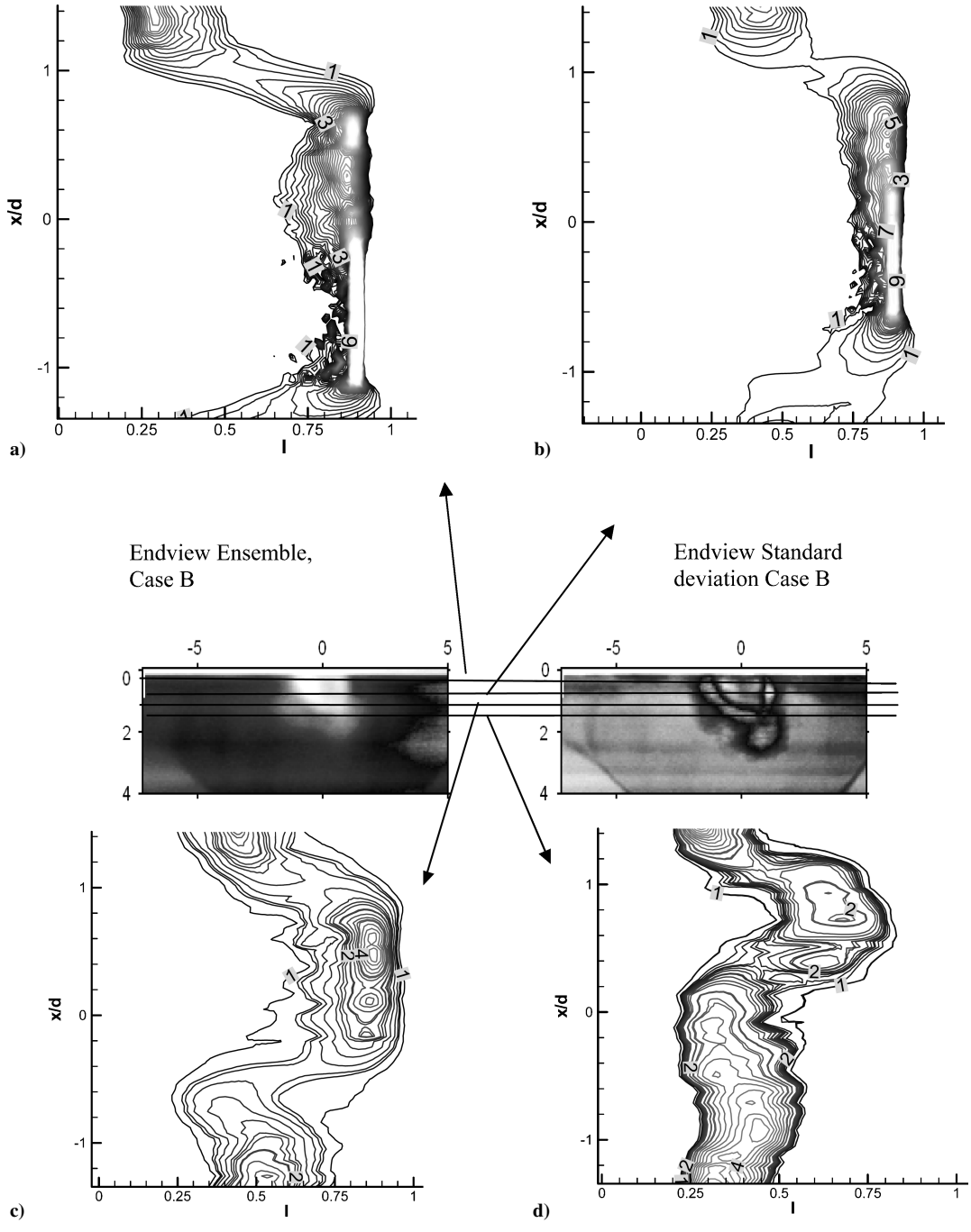

Fig. 15 End-view PDFs contours for case B from Mie scatter: a) $y/d = 0.31$, b) $y/d = 0.94$, c) $y/d = 1.2$, and d) $y/d = 1.6$.

sides of the jet at all transverse locations studied. The lower half ($x/d < 0$) of the plot (Fig. 15a) indicates high probability of jet fluid and a well-defined boundary, whereas the top half ($x/d > 0$) has a mixture of jet and mixed fluid at $y/d = 0.31$. The jet became more symmetric at $y/d = 0.94$, but there is still an unequal probability distribution of the fluid mixture fraction. The lower half had a higher probability of high density jet fluid at $y/d = 0.94$, whereas at $y/d = 1.2$ it shows a reverse trend. The probability of finding high-density jet fluid also decreased at $y/d = 1.2$ near the core, which indicates that the jet fluid became well mixed with the freestream. At $y/d = 1.6$, the PDF contour shifted toward the lower probability, but the upper half is skewed toward the high-density side. Asymmetry of swirling jet in crossflow has also been observed by other investigators from their mean concentration[28,30] and pressure distribution measurements.[29] The end-view PDF contours also support this observation of skewness of a swirling jet in crossflow in a dynamic sense.

Conclusions

Transverse injection of a swirling supersonic injector with a central control jet into a $M = 2$ cold crossflow was studied using NO–PLIF and Rayleigh/Mie scattering. The jet windward boundary trajectory scaled with a power law fit as observed in low-speed flows. Control case A showed a steady increase in penetration slope as compared to a circular injector. It had a 58% increase in slope compared to the transverse circular jet. Control cases B and C showed improved penetration over a swirling baseline injector but were lower than the circular jet. There was a 16% increase in standard deviation of the mixing area region identified from the side-view images ($A_{,\sigma 30}/A_{\text{jet}} >= 30\%$) past 7.4 jet diameters for case B when compared to case A. PDFs from side-view images were used to study the probability of identifying different mixture fraction within the mixing layer. The PDF contours at different streamwise locations indicated that it could be used as a measure to track the jet centerline and the two boundaries on a dynamic scale. For cases A–C in which both the central and swirling jet were on, the jet centerline trajectory identified from the PDF contours did not match the time-averaged jet trajectory for several cases at different axial locations. The PDF marker considers the dynamic nature of the turbulent transverse jet, whereas the time-averaged markers could be smeared due to averaging. Cases A and C show intermittency of finding high-density jet mixed and freestream fluid at $x = 4.6$ jet diameters along the transverse direction, whereas case B shows a more uniform mixed fluid at the same axial location. Both the time-averaged and standard deviation end-view images show an elliptical jet boundary for case B as compared to case A and C. Δz_{std}, A_{mean}, and Δz_{mean} obtained from end-view instantaneous images for control cases A–C have higher fluctuation of the spanwise jet boundary, larger area, and higher jet width along the spanwise direction when compared to the baseline swirling and circular jets.

The current study indicates that the CSSI is capable of achieving good mixing and entrainment while maintaining high penetration when compared to the swirling baseline and circular jet transverse injection. The CSSI provides as a suitable alternative over a circular nozzle for use as an injector in a scramjet combustor because it provides the benefit of controlling both the penetration and growth rate independently. This provides the means to tailor the local fuel equivalence ratio and, thus, to control the global heat release distribution. A cluster of CSSI installed at a single location can reduce the number of fuel injection sites, thereby simplifying the plumbing associated with the fuel lines. The CSSI can be angled with respect to the crossflow to reduce penalty associated with shock losses without compromising the efficiency.

Acknowledgments

The financial support of the Dayton Area Graduate Studies Institute Program is gratefully appreciated. The authors acknowledge Dave Schommer and Bill Terry at Innovative Scientific Solutions, Inc., for their help and support in setting up the experiments.

References

[1]Lee, M. P., McMillin, B. K., Palmer, J. L., and Hanson, R. K., "Planar Fluorescence Imaging of a Transverse Jet in a Supersonic Cross Flow," *Journal of Propulsion and Power*, Vol. 8, No. 4, 1992, pp. 729–735.

[2]Hermanson, J. C., and Winter, M., "Mie Scattering Imaging of Transverse, Sonic Jet in Supersonic Flow," *AIAA Journal*, Vol. 31, No. 1, 1993, pp. 129–132.

[3]Gruber, M. R., Nejad, A. S., Chen, T. H., and Dutton, J. C., "Transverse Injection from Circular and Elliptic Nozzles into a Supersonic Crossflow," *Journal of Propulsion and Power*, Vol. 16, No. 8, 2000, pp. 449–457.

[4]VanLerberghe, W. M., Santiago, J. G., Dutton, J. C., and Lucht, R. P., "Mixing of a Sonic Transverse Jet injected into a Supersonic Flow," *AIAA Journal*, Vol. 38, No. 3, 2000, pp. 470–479.

[5]Northam, G. B., Greenberg, I., and Byington, C. S., "Evaluation of Parallel Injector Configurations for Supersonic Combustion," AIAA Paper 89-2525, 1989.

[6]Gutmark, E. J., Schadow, K. C., and Yu, K. H., "Mixing Enhancement in Supersonic Free Shear Flows," *Annual Review of Fluid Mechanics*, Vol. 27, 1995, pp. 375–417.

[7]Seiner, J. M., Dash, S. M., and Kenzakowski, D. C., "Historical Survey on Enhanced Mixing in Scramjet Engines," *Journal of Propulsion and Power*, Vol. 17, No. 6, 2001, pp. 1273–1286.

[8]Bogdanoff, D. W., "Advanced Injection and Mixing Techniques for Scramjet Combustors," *Journal of Propulsion and Power*, Vol. 10, No. 2, 1994, pp. 183–190.

[9]Bushnell, D. M., "Hypervelocity Scramjet Mixing Enhancement," *Journal of Propulsion and Power*, Vol. 11, No. 5, 1994, pp. 1088–1090.

[10]Marble, F. E., Zukoski, E. E., Jacobs, J. W., Hendrick, G. J., and Waitz, I. A., "Shock Enhancement of and Control of Hypersonic Mixing and Combustion," AIAA Paper 90-1981, April 1990.

[11]Elliott, J. K., Manning, T. A., Qiu, Y. J., Greitzer, E. M., Tan, C. S., and Tillman, T. G., "Computational and Experimental Studies of Flow in a Multi-Lobes Forced Mixers," AIAA Paper 92-3568, 1992.

[12]Presz, W. M., Gousy, R., and Morin, B. L., "Forced Mixer Lobes in Ejector Designs," *Journal of Propulsion and Power*, Vol. 4, No. 4, 1988, pp. 350–355.

[13]Tillman, T. G., Patterson, R. W., and Presz, W. M., Jr., "Supersonic Nozzle Mixer Ejector," *Journal of Propulsion and Power*, Vol. 8, No. 2, 1992, pp. 513–519.

[14]Drummond, J. P., Carpenter, M. H., and Riggins, D. W., "Mixing and Mixing Enhancement in Supersonic Reacting Flowfields," *High-Speed Flight Propulsion Systems*, Vol. 137, Progress in Astronautics and Aeronautics, AIAA, Washington, DC, 1991, pp. 383–455.

[15]Rogers, R. C., Capriotti, D. P., and Guy, R. W., "Experimental Supersonic Combustion Research at NASA Langley," AIAA Paper 98-2506, June 1998.

[16]Stouffer, S. D., Baker, N. R., Capriotti, D. P., and Northam, G. B., "Effects of Compression and Expansion Ramp Fuel Injector Configurations on Scramjet Combustion and Heat Transfer," AIAA Paper 93-0609, 1993.

[17]Papamoschou, D., "Structure of the Compressible Turbulent Shear Layer," *AIAA Journal*, Vol. 29, No. 5, 1991, pp. 680, 681.

[18]Fernando, E. M., and Menon, S., "Mixing Enhancement in Compressible Mixing Layers: An Experimental Study," *AIAA Journal*, Vol. 31, No. 2, 1993, pp. 278–285.

[19]Seiner, J. M., and Grosch, C. E., "Effect of Tabs on Mixing on Round Jets," AIAA/Confederation of European Aerospace Societies Aeroacoustics, Paper 98-2326, June 1998.

[20]Ahuja, K. K., and Brown, W. H., "Shear Flow Control by Mechanical Tabs," AIAA Paper 89-0994, Jan. 1989.

[21]Zaman, K. B. M. Q., Reeder, M. F., and Samimy, M., "Control of an Axisymmetric Jet Using Vortex Generators," *Physics of Fluids*, Vol. 6, No. 2, 1994, pp. 778–793.

[22]Grosch, C. E., Seiner, J. M., Hussaini, M. Y., and Jackson, T. L., "Numerical Simulation of Mixing Enhancement in a Hot Supersonic Jet," *Physics of Fluids*, Vol. 9, No. 4, 1997, pp. 1125–1143.

[23]Schadow, K. C., and Gutmark, E., "Review of Passive Shear-Flow Control Research for Improved Subsonic and Supersonic Combustion," AIAA Paper 89-2786, 1989.

[24]Pannus, S. S., and Johannesen, N. H., "The Structure of Jets from Notched Nozzle," *Journal of Fluid Mechanics*, Vol. 74, No. 3, 1976, pp. 515–528.

[25]Tillman, T. G., Patrick, W. P., and Paterson, R. W., "Enhanced Mixing of Supersonic Jets," *Journal of Propulsion and Power*, Vol. 7, No. 6, 1991, pp. 1006–1014.

[26]Syred, N., and Beer, J. M., "Combustion in Swirling Flows: A Review," *Combustion and Flame*, Vol. 23, Oct. 1974, pp. 143–201.

[27]Naughton, J. W., Cattafesta, L. N., and Settles, G. S., "An Experimental Study of Compressible Turbulent Mixing Enhancement in Swirling jets," *Journal of Fluid Mechanics*, Vol. 30, 1997, pp. 271–305.

[28]Cutler, A. D., and Doerner, S. E., "Effects of Swirl and Skew upon Supersonic Wall Jet in Cross Flow," *Journal of Propulsion and Power*, Vol. 17, No. 6, 2001, pp. 1327–1332.

[29]Kavsaoglu, M. S., and Schetz, J. A., "Effects of Swirl and High Turbulence on a Jet in a Crossflow," *Journal of Aircraft*, Vol. 26, No. 6, 1989, pp. 539–546.

[30]Niederhaus, C. E., Champagne, F. H., and Jacobs, J. W., "Scalar Transport in a Swirling Transverse Jet," *AIAA Journal*, Vol. 35, No. 11, 1997, pp. 1697–1704.

[31]Gruber, M. R., and Nejad, A. S., "New Supersonic Combustion Research Facility," *Journal of Propulsion and Power*, Vol. 11, No. 5, 1995, pp. 1080–1083.

[32]Gupta, A. K., Lilley, D. G., and Syred, N., *Swirl Flows*, Abacus, London, 1984.

[33]Murugappan, S., and Gutmark, E., "A Novel Swirling Injector for Improving Mixing in High Speed Flows," AIAA Paper 2003-4785, 2003.

[34]Orth, R. C., Schetz, J. A., and Billig, F. S., "The Interaction and Penetration of Gaseous Jets in Supersonic Flow," NASA CR -1386, July 1969.

[35]Papamoschou, D., and Hubbard, D. G., "Visual Observations of Supersonic Transverse Jets," *Experiments in Fluids*, Vol. 14, No. 6, 1993, pp. 468–476.

[36]Dowling, D. R., and Dimotakis, P. E., "Similarity of the Concentration Field of Gas Phase Turbulent Jets," *Journal of Fluid Mechanics*, Vol. 218, 1990, pp. 109–142.

[37]Clemens, N. T., and Mungal, M. G., "Large-Scale Structure and Entrainment in the Supersonic Mixing Layer," *Journal of Fluid Mechanics*, Vol. 284, 1995, pp. 171–216.

[38]Smith, S. H., and Mungal, M. G., "Mixing, Structure and Scaling of the Jet in Crossflow," *Journal of Fluid Mechanics*, Vol. 357, 1998, pp. 83–122.

[39]Pratte, B. D., and Baines, W. D., "Profiles of Round Turbulent Jet in Cross Flow," *Journal of Hydronautics*, Vol. 92, 1967, pp. 53–64.

[40]Wang, K. C., Smith, O. I., Karagozian, A. R., "In-Flight Imaging Gas Jets Injected into Compressible Crossflows," *AIAA Journal*, Vol. 33, No. 12, 1995, pp. 2259–2263.

[41]Messersmith, N. L., and Dutton, J. C., "Mie Scattering Measurements of Probability Density Functions in Compressible Mixing Layers," *Experiments in Fluids*, Vol. 21, No. 4, 1996, pp. 291–301.

[42]Clemens, N. T., and Mungal, M. G., "Large- Scale Structure and Entrainment in the Supersonic Mixing Layer," *Journal of Fluid Mechanics*, Vol. 284, 1995, pp. 171–216.

[43]Konrad, J. H., "An Experimental Investigation of Mixing in Two Dimensional Turbulent Shear Flowswith Applications to Diffusion Limited Chemical Reactions," Ph.D. Dissertation, Dept. of Aeronautics, California Inst. of Technology, Pasadena, CA, 1977.

[44]Rajagopalan, S., and Antonia, R. A., "Properties of the Large Structure in a Slightly Heated Turbulent Mixing Layer of a Plane Jet," *Journal of Fluid Mechanics*, Vol. 105, 1981, pp. 261–281.

[45]Kamotani, Y., and Greber, I., "Experiments on a Turbulent Jet in Cross Flow," *AIAA Journal*, Vol. 10, No.11, 1972, pp. 1425–1429.

[46]Haniu, H., and Ramaprian, B. R., "Studies on Two-Dimensional Curved Nonbuoyant Jets in Cross Flow," *Journal of Fluids Engineering*, Vol. 111, 1989, pp. 78–86.

A. Karagozian
Associate Editor